Title	ϕ meson production in the forward/backward rapidity region in Cu + Au collisions at $\sqrt{sNN}=200$ GeV
Author(s)	Adare A., Hasegawa Shoichi, Imai Kenichi, Nagamiya Shoji, Sako Hiroyuki, Sato Susumu, Tanida Kiyoshi, PHENIX Collaboration, 505 of others
Citation	Physical Review C, 93(2), p.024904_1-024904_13
Text Version	Publisher's Version
URL	https://jopss.jaea.go.jp/search/servlet/search?5055619
DOI	https://doi.org/10.1103/PhysRevC.93.024904
Right	

ϕ meson production in the forward/backward rapidity region in Cu + Au collisions at $\sqrt{s_{NN}} = 200$ GeV

A. Adare,[13] C. Aidala,[39,44] N. N. Ajitanand,[64] Y. Akiba,[58,59] R. Akimoto,[12] J. Alexander,[64] M. Alfred,[23] H. Al-Ta'ani,[52] K. R. Andrews,[1] A. Angerami,[14] K. Aoki,[32,58] N. Apadula,[28,65] E. Appelt,[69] Y. Aramaki,[12,58] R. Armendariz,[8] H. Asano,[35,58] E. C. Aschenauer,[7] E. T. Atomssa,[65] T. C. Awes,[54] B. Azmoun,[7] V. Babintsev,[24] M. Bai,[6] X. Bai,[11] N. S. Bandara,[43] B. Bannier,[65] K. N. Barish,[8] B. Bassalleck,[51] A. T. Basye,[1] S. Bathe,[5,59] V. Baublis,[57] C. Baumann,[7,45] S. Baumgart,[58] A. Bazilevsky,[7] M. Beaumier,[8] S. Beckman,[13] R. Belmont,[13,44,69] J. Ben-Benjamin,[46] R. Bennett,[65] A. Berdnikov,[61] Y. Berdnikov,[61] D. Black,[8] D. S. Blau,[34] J. S. Bok,[52,72] K. Boyle,[59] M. L. Brooks,[39] D. Broxmeyer,[46] J. Bryslawskyj,[5] H. Buesching,[7] V. Bumazhnov,[24] G. Bunce,[7,59] S. Butsyk,[39,51] S. Campbell,[14,28,65] P. Castera,[65] C.-H. Chen,[59,65] C. Y. Chi,[14] M. Chiu,[7] I. J. Choi,[25,72] J. B. Choi,[10] S. Choi,[63] R. K. Choudhury,[4] P. Christiansen,[41] T. Chujo,[68] O. Chvala,[8] V. Cianciolo,[54] Z. Citron,[65,70] B. A. Cole,[14] Z. Conesa del Valle,[36] M. Connors,[65] N. Cronin,[46,65] N. Crossette,[46] M. Csanád,[17] T. Csörgő,[71] S. Dairaku,[35,58] T. W. Danley,[53] A. Datta,[43,51] M. S. Daugherity,[1] G. David,[7] M. K. Dayananda,[20] K. DeBlasio,[51] K. Dehmelt,[65] A. Denisov,[24] A. Deshpande,[59,65] E. J. Desmond,[7] K. V. Dharmawardane,[52] O. Dietzsch,[62] L. Ding,[28] A. Dion,[28,65] P. B. Diss,[42] J. H. Do,[72] M. Donadelli,[62] L. D'Orazio,[42] O. Drapier,[36] A. Drees,[65] K. A. Drees,[6] J. M. Durham,[39,65] A. Durum,[24] Y. V. Efremenko,[54] T. Engelmore,[14] A. Enokizono,[54,58,60] H. En'yo,[58,59] S. Esumi,[68] K. O. Eyser,[7] B. Fadem,[46] N. Feege,[65] D. E. Fields,[51] M. Finger,[9] M. Finger, Jr.,[9] F. Fleuret,[36] S. L. Fokin,[34] J. E. Frantz,[53] A. Franz,[7] A. D. Frawley,[19] Y. Fukao,[32,58] T. Fusayasu,[48] K. Gainey,[1] C. Gal,[65] P. Gallus,[15] P. Garg,[3] A. Garishvili,[66] I. Garishvili,[38,66] H. Ge,[65] F. Giordano,[25] A. Glenn,[38] X. Gong,[64] M. Gonin,[36] Y. Goto,[58,59] R. Granier de Cassagnac,[36] N. Grau,[2,14] S. V. Greene,[69] M. Grosse Perdekamp,[25] Y. Gu,[64] T. Gunji,[12] L. Guo,[39] H. Guragain,[20] H.-Å. Gustafsson,[41,*] T. Hachiya,[58] J. S. Haggerty,[7] K. I. Hahn,[18] H. Hamagaki,[12] J. Hamblen,[66] H. F. Hamilton,[1] R. Han,[56] S. Y. Han,[18] J. Hanks,[14,65] C. Harper,[46] S. Hasegawa,[29] T. O. S. Haseler,[20] K. Hashimoto,[58,60] E. Haslum,[41] R. Hayano,[12] X. He,[20] T. K. Hemmick,[65] T. Hester,[8] J. C. Hill,[28] R. S. Hollis,[8] W. Holzmann,[14] K. Homma,[22] B. Hong,[33] T. Horaguchi,[68] Y. Hori,[12] D. Hornback,[54] T. Hoshino,[22] N. Hotvedt,[28] J. Huang,[7,39] S. Huang,[69] T. Ichihara,[58,59] R. Ichimiya,[58] H. Iinuma,[32] Y. Ikeda,[58,68] K. Imai,[29,35,58] Y. Imazu,[58] M. Inaba,[68] A. Iordanova,[8] D. Isenhower,[1] M. Ishihara,[58] A. Isinhue,[46] M. Issah,[69] D. Ivanishchev,[57] Y. Iwanaga,[22] B. V. Jacak,[65] S. J. Jeon,[47] M. Jezghani,[20] J. Jia,[7,64] X. Jiang,[39] D. John,[66] B. M. Johnson,[7] T. Jones,[1] K. S. Joo,[47] D. Jouan,[55] D. S. Jumper,[25] J. Kamin,[65] S. Kanda,[12,32] S. Kaneti,[65] B. H. Kang,[21] J. H. Kang,[72] J. S. Kang,[21] J. Kapustinsky,[39] K. Karatsu,[35,58] M. Kasai,[58,60] D. Kawall,[43,59] A. V. Kazantsev,[34] T. Kempel,[28] J. A. Key,[51] V. Khachatryan,[65] P. K. Khandai,[3] A. Khanzadeev,[57] K. M. Kijima,[22] B. I. Kim,[33] C. Kim,[33] D. J. Kim,[30] E.-J. Kim,[10] G. W. Kim,[18] M. Kim,[63] Y.-J. Kim,[25] Y. K. Kim,[21] B. Kimelman,[46] E. Kinney,[13] Á. Kiss,[17] E. Kistenev,[7] R. Kitamura,[12] J. Klatsky,[19] D. Kleinjan,[8] P. Kline,[65] T. Koblesky,[13] L. Kochenda,[57] M. Kofarago,[17] B. Komkov,[57] M. Konno,[68] J. Koster,[25,59] D. Kotchetkov,[53] D. Kotov,[57,61] A. Král,[15] F. Krizek,[30] G. J. Kunde,[39] K. Kurita,[58,60] M. Kurosawa,[58,59] Y. Kwon,[72] G. S. Kyle,[52] R. Lacey,[64] Y. S. Lai,[14] J. G. Lajoie,[28] A. Lebedev,[28] D. M. Lee,[39] G. H. Lee,[10] J. Lee,[18] K. B. Lee,[33,39] K. S. Lee,[33] S. Lee,[72] S. H. Lee,[65] S. R. Lee,[10] M. J. Leitch,[39] M. A. L. Leite,[62] M. Leitgab,[25] B. Lewis,[65] X. Li,[11] S. H. Lim,[72] L. A. Linden Levy,[13] H. Liu,[39] M. X. Liu,[39] B. Love,[69] D. Lynch,[7] C. F. Maguire,[69] Y. I. Makdisi,[6] M. Makek,[70,73] A. Manion,[65] V. I. Manko,[34] E. Mannel,[7,14] Y. Mao,[56,58] T. Maruyama,[29] H. Masui,[68] M. McCumber,[13,39,65] P. L. McGaughey,[39] D. McGlinchey,[13,19] C. McKinney,[25] N. Means,[65] A. Meles,[52] M. Mendoza,[8] B. Meredith,[25] Y. Miake,[68] T. Mibe,[32] A. C. Mignerey,[42] K. Miki,[58,68] A. Milov,[70] D. K. Mishra,[4] J. T. Mitchell,[7] Y. Miyachi,[58,67] S. Miyasaka,[58,67] S. Mizuno,[58,68] A. K. Mohanty,[4] S. Mohapatra,[64] P. Montuenga,[25] H. J. Moon,[47] T. Moon,[72] Y. Morino,[12] A. Morreale,[8] D. P. Morrison,[7,†] M. Moskowitz,[46] S. Motschwiller,[46] T. V. Moukhanova,[34] T. Murakami,[35,58] J. Murata,[58,60] A. Mwai,[64] T. Nagae,[35] S. Nagamiya,[32,58] K. Nagashima,[22] J. L. Nagle,[13,‡] M. Naglis,[70] M. I. Nagy,[17,71] I. Nakagawa,[58,59] H. Nakagomi,[58,68] Y. Nakamiya,[22] K. R. Nakamura,[35,58] T. Nakamura,[58] K. Nakano,[58,67] C. Nattrass,[66] P. K. Netrakanti,[4] J. Newby,[38] M. Nguyen,[65] M. Nihashi,[22,58] T. Niida,[68] S. Nishimura,[12] R. Nouicer,[7,59] T. Novák,[31,71] N. Novitzky,[30,65] A. S. Nyanin,[34] C. Oakley,[20] E. O'Brien,[7] C. A. Ogilvie,[28] H. Oide,[12] M. Oka,[68] K. Okada,[59] J. D. Orjuela Koop,[13] J. D. Osborn,[44] A. Oskarsson,[41] M. Ouchida,[22,58] K. Ozawa,[12,32] R. Pak,[7] V. Pantuev,[26,65] V. Papavassiliou,[52] B. H. Park,[21] I. H. Park,[18] J. S. Park,[63] S. Park,[63] S. K. Park,[33] S. F. Pate,[52] L. Patel,[20] M. Patel,[28] H. Pei,[28] J.-C. Peng,[25] H. Pereira,[16] D. V. Perepelitsa,[7,14] G. D. N. Perera,[52] D. Yu. Peressounko,[34] J. Perry,[28] R. Petti,[7,65] C. Pinkenburg,[7] R. Pinson,[1] R. P. Pisani,[7] M. Proissl,[65] M. L. Purschke,[7] H. Qu,[1,20] J. Rak,[30] B. J. Ramson,[44] I. Ravinovich,[70] K. F. Read,[54,66] K. Reygers,[45] D. Reynolds,[64] V. Riabov,[50,57] Y. Riabov,[57,61] E. Richardson,[42] T. Rinn,[28] N. Riveli,[53] D. Roach,[69] G. Roche,[40,*] S. D. Rolnick,[8] M. Rosati,[28] S. S. E. Rosendahl,[41] Z. Rowan,[5] J. G. Rubin,[44] M. S. Ryu,[21] B. Sahlmueller,[45,65] N. Saito,[32] T. Sakaguchi,[7] H. Sako,[29] V. Samsonov,[50,57] S. Sano,[12] M. Sarsour,[20] S. Sato,[29] T. Sato,[68] M. Savastio,[65] S. Sawada,[32] B. Schaefer,[69] B. K. Schmoll,[66] K. Sedgwick,[8] J. Seele,[59] R. Seidl,[58,59] Y. Sekiguchi,[12] A. Sen,[20,66] R. Seto,[8] P. Sett,[4] A. Sexton,[42] D. Sharma,[65,70] A. Shaver,[28] I. Shein,[24] T.-A. Shibata,[58,67] K. Shigaki,[22] H. H. Shim,[33] M. Shimomura,[28,49,68] K. Shoji,[35,58] P. Shukla,[4] A. Sickles,[7,25] C. L. Silva,[28,39] D. Silvermyr,[41,54] C. Silvestre,[16] K. S. Sim,[33] B. K. Singh,[3] C. P. Singh,[3] V. Singh,[3] M. Skolnik,[46] M. Slunečka,[9] M. Snowball,[39] T. Sodre,[46] S. Solano,[46] R. A. Soltz,[38] W. E. Sondheim,[39] S. P. Sorensen,[66] I. V. Sourikova,[7] P. W. Stankus,[54] P. Steinberg,[7] E. Stenlund,[41] M. Stepanov,[43,52,*] A. Ster,[71] S. P. Stoll,[7] M. R. Stone,[13] T. Sugitate,[22] A. Sukhanov,[7] T. Sumita,[58] J. Sun,[65] J. Sziklai,[71] E. M. Takagui,[62] A. Takahara,[12] A. Taketani,[58,59] R. Tanabe,[68] Y. Tanaka,[48] S. Taneja,[65] K. Tanida,[35,58,59,63] M. J. Tannenbaum,[7] S. Tarafdar,[3,70] A. Taranenko,[50,64] E. Tennant,[52] H. Themann,[65] D. Thomas,[1] R. Tieulent,[20] A. Timilsina,[28]

T. Todoroki,[58,68] M. Togawa,[59] L. Tomášek,[27] M. Tomášek,[15,27] H. Torii,[12,22] C. L. Towell,[1] R. Towell,[1] R. S. Towell,[1] I. Tserruya,[70] Y. Tsuchimoto,[22] K. Utsunomiya,[12] C. Vale,[7] H. W. van Hecke,[39] M. Vargyas,[17] E. Vazquez-Zambrano,[14] A. Veicht,[14] J. Velkovska,[69] R. Vértesi,[71] M. Virius,[15] A. Vossen,[25] V. Vrba,[15,27] E. Vznuzdaev,[57] X. R. Wang,[52,59] D. Watanabe,[22] K. Watanabe,[58,60,68] Y. Watanabe,[58,59] Y. S. Watanabe,[12,32] F. Wei,[28,52] R. Wei,[64] J. Wessels,[45] S. Whitaker,[28] A. S. White,[44] S. N. White,[7] D. Winter,[14] S. Wolin,[25] C. L. Woody,[7] R. M. Wright,[1] M. Wysocki,[13,54] B. Xia,[53] L. Xue,[20] S. Yalcin,[65] Y. L. Yamaguchi,[12,58,65] R. Yang,[25] A. Yanovich,[24] J. Ying,[20] S. Yokkaichi,[58,59] J. H. Yoo,[33] J. S. Yoo,[18] I. Yoon,[63] Z. You,[39,56] G. R. Young,[54] I. Younus,[37,51] H. Yu,[56] I. E. Yushmanov,[34] W. A. Zajc,[14] A. Zelenski,[6] S. Zhou,[11] and L. Zou[8]

(PHENIX Collaboration)

[1]*Abilene Christian University, Abilene, Texas 79699, USA*

[2]*Department of Physics, Augustana University, Sioux Falls, South Dakota 57197, USA*

[3]*Department of Physics, Banaras Hindu University, Varanasi 221005, India*

[4]*Bhabha Atomic Research Centre, Bombay 400 085, India*

[5]*Baruch College, City University of New York, New York, New York 10010, USA*

[6]*Collider-Accelerator Department, Brookhaven National Laboratory, Upton, New York 11973-5000, USA*

[7]*Physics Department, Brookhaven National Laboratory, Upton, New York 11973-5000, USA*

[8]*University of California-Riverside, Riverside, California 92521, USA*

[9]*Charles University, Ovocný trh 5, Praha 1, 116 36, Prague, Czech Republic*

[10]*Chonbuk National University, Jeonju 561-756, Korea*

[11]*Science and Technology on Nuclear Data Laboratory, China Institute of Atomic Energy, Beijing 102413, People's Republic of China*

[12]*Center for Nuclear Study, Graduate School of Science, University of Tokyo, 7-3-1 Hongo, Bunkyo, Tokyo 113-0033, Japan*

[13]*University of Colorado, Boulder, Colorado 80309, USA*

[14]*Columbia University, New York, New York 10027, USA and Nevis Laboratories, Irvington, New York 10533, USA*

[15]*Czech Technical University, Zikova 4, 166 36 Prague 6, Czech Republic*

[16]*Dapnia, CEA Saclay, F-91191 Gif-sur-Yvette, France*

[17]*ELTE, Eötvös Loránd University, H-1117 Budapest, Pázmány P. s. 1/A, Hungary*

[18]*Ewha Womans University, Seoul 120-750, Korea*

[19]*Florida State University, Tallahassee, Florida 32306, USA*

[20]*Georgia State University, Atlanta, Georgia 30303, USA*

[21]*Hanyang University, Seoul 133-792, Korea*

[22]*Hiroshima University, Kagamiyama, Higashi-Hiroshima 739-8526, Japan*

[23]*Department of Physics and Astronomy, Howard University, Washington, DC 20059, USA*

[24]*IHEP Protvino, State Research Center of Russian Federation, Institute for High Energy Physics, Protvino 142281, Russia*

[25]*University of Illinois at Urbana-Champaign, Urbana, Illinois 61801, USA*

[26]*Institute for Nuclear Research of the Russian Academy of Sciences, prospekt 60-letiya Oktyabrya 7a, Moscow 117312, Russia*

[27]*Institute of Physics, Academy of Sciences of the Czech Republic, Na Slovance 2, 182 21 Prague 8, Czech Republic*

[28]*Iowa State University, Ames, Iowa 50011, USA*

[29]*Advanced Science Research Center, Japan Atomic Energy Agency, 2-4 Shirakata Shirane, Tokai-mura, Naka-gun, Ibaraki-ken 319-1195, Japan*

[30]*Helsinki Institute of Physics and University of Jyväskylä, P.O. Box 35, FI-40014 Jyväskylä, Finland*

[31]*Károly Róberts University College, H-3200 Gyöngyös, Mátraiút 36, Hungary*

[32]*KEK, High Energy Accelerator Research Organization, Tsukuba, Ibaraki 305-0801, Japan*

[33]*Korea University, Seoul 136-701, Korea*

[34]*National Research Center "Kurchatov Institute," Moscow 123098 Russia*

[35]*Kyoto University, Kyoto 606-8502, Japan*

[36]*Laboratoire Leprince-Ringuet, Ecole Polytechnique, CNRS-IN2P3, Route de Saclay F-91128, Palaiseau, France*

[37]*Physics Department, Lahore University of Management Sciences, Lahore 54792, Pakistan*

[38]*Lawrence Livermore National Laboratory, Livermore, California 94550, USA*

[39]*Los Alamos National Laboratory, Los Alamos, New Mexico 87545, USA*

[40]*LPC, Université Blaise Pascal, CNRS-IN2P3, Clermont-Fd, 63177 Aubiere Cedex, France*

[41]*Department of Physics, Lund University, Box 118, SE-221 00 Lund, Sweden*

[42]*University of Maryland, College Park, Maryland 20742, USA*

[43]*Department of Physics, University of Massachusetts, Amherst, Massachusetts 01003-9337, USA*

[44]*Department of Physics, University of Michigan, Ann Arbor, Michigan 48109-1040, USA*

[45]*Institut für Kernphysik, University of Muenster, D-48149 Muenster, Germany*

[46]*Muhlenberg College, Allentown, Pennsylvania 18104-5586, USA*

[47]*Myongji University, Yongin, Kyonggido 449-728, Korea*

[48]*Nagasaki Institute of Applied Science, Nagasaki-shi, Nagasaki 851-0193, Japan*

[49]*Nara Women's University, Kita-uoya Nishi-machi Nara 630-8506, Japan*

[50]*National Research Nuclear University, MEPhI, Moscow Engineering Physics Institute, Moscow 115409, Russia*
[51]*University of New Mexico, Albuquerque, New Mexico 87131, USA*
[52]*New Mexico State University, Las Cruces, New Mexico 88003, USA*
[53]*Department of Physics and Astronomy, Ohio University, Athens, Ohio 45701, USA*
[54]*Oak Ridge National Laboratory, Oak Ridge, Tennessee 37831, USA*
[55]*IPN-Orsay, Univ. Paris-Sud, CNRS/IN2P3, Université Paris-Saclay, BP1, F-91406 Orsay, France*
[56]*Peking University, Beijing 100871, People's Republic of China*
[57]*PNPI, Petersburg Nuclear Physics Institute, Gatchina, Leningrad Region 188300, Russia*
[58]*RIKEN Nishina Center for Accelerator-Based Science, Wako, Saitama 351-0198, Japan*
[59]*RIKEN BNL Research Center, Brookhaven National Laboratory, Upton, New York 11973-5000, USA*
[60]*Physics Department, Rikkyo University, 3-34-1 Nishi-Ikebukuro, Toshima, Tokyo 171-8501, Japan*
[61]*Saint Petersburg State Polytechnic University, St. Petersburg 195251, Russia*
[62]*Universidade de São Paulo, Instituto de Física, Caixa Postal 66318, São Paulo CEP05315-970, Brazil*
[63]*Department of Physics and Astronomy, Seoul National University, Seoul 151-742, Korea*
[64]*Chemistry Department, Stony Brook University, SUNY, Stony Brook, New York 11794-3400, USA*
[65]*Department of Physics and Astronomy, Stony Brook University, SUNY, Stony Brook, New York 11794-3800, USA*
[66]*University of Tennessee, Knoxville, Tennessee 37996, USA*
[67]*Department of Physics, Tokyo Institute of Technology, Oh-okayama, Meguro, Tokyo 152-8551, Japan*
[68]*Center for Integrated Research in Fundamental Science and Engineering, University of Tsukuba, Tsukuba, Ibaraki 305, Japan*
[69]*Vanderbilt University, Nashville, Tennessee 37235, USA*
[70]*Weizmann Institute, Rehovot 76100, Israel*
[71]*Institute for Particle and Nuclear Physics, Wigner Research Centre for Physics, Hungarian Academy of Sciences (Wigner RCP, RMKI) H-1525 Budapest 114, P.O. Box 49, Budapest, Hungary*
[72]*Yonsei University, IPAP, Seoul 120-749, Korea*
[73]*University of Zagreb, Faculty of Science, Department of Physics, Bijenička 32, HR-10002 Zagreb, Croatia*
(Received 5 October 2015; published 4 February 2016)

The PHENIX experiment at the Relativistic Heavy Ion Collider has measured ϕ meson production and its nuclear modification in asymmetric Cu + Au heavy-ion collisions at $\sqrt{s_{NN}} = 200$ GeV at both forward Cu-going direction ($1.2 < y < 2.2$) and backward Au-going direction ($-2.2 < y < -1.2$) rapidities. The measurements are performed via the dimuon decay channel and reported as a function of the number of participating nucleons, rapidity, and transverse momentum. In the most central events, 0%–20% centrality, the ϕ meson yield integrated over $1 < p_T < 5$ GeV/c prefers a smaller value, which means a larger nuclear modification, in the Cu-going direction compared to the Au-going direction. Additionally, the nuclear-modification factor in Cu + Au collisions averaged over all centrality is measured to be similar to the previous PHENIX result in d + Au collisions for these rapidities.

DOI: 10.1103/PhysRevC.93.024904

I. INTRODUCTION

The Relativistic Heavy Ion Collider (RHIC) accelerator and its four experiments have previously provided extensive experimental evidence to confirm the formation of a deconfined state of nuclear matter, referred to as the quark-gluon plasma (QGP), in the initial stages of high-energy heavy-ion collisions [1–4]. Currently, a major objective in the field of high-energy nuclear physics is to characterize the properties of the QGP in a quantitative way. The ϕ meson is a useful probe for studying the QGP properties because it is sensitive to several aspects of the collision, including modifications of strangeness production in bulk matter [5–7]. Owing to its small inelastic cross section for interaction with nonstrange hadrons [6,8], the ϕ meson is less affected by late hadronic rescattering and may reflect the initial evolution of the system. Being composed of a nearly pure strange antistrange ($s\bar{s}$) state, the ϕ meson puts additional constraints on models of quark recombination in the QGP.

The study of the QGP typically involves comparisons of different observables measured in nucleus-nucleus (A + B) collisions and in proton-proton ($p + p$) collisions at the same center-of-mass energy. Modifications in the A + B collisions with respect to $p + p$ collisions could be interpreted as being attributable to the hot nuclear matter (HNM)—possibly QGP—being produced. However, nuclear modifications could be present in the initial state of the collisions even if no QGP is produced. These effects, typically referred to as cold nuclear matter (CNM), may include the modification of parton distribution functions (PDFs) in a nucleus [9], initial-state energy loss [10], and the Cronin effect, which is often attributed to multiple scattering of the incoming parton inside the target nucleus [11,12]. CNM effects can be probed with d + Au collisions. PHENIX has previously measured ϕ meson production in d + Au collisions at forward, mid-,

*Deceased
†PHENIX Cospokesperson: morrison@bnl.gov
‡PHENIX Cospokesperson: jamie.nagle@colorado.edu

and backward rapidities [13]. Suppression was observed in the forward (d-going) direction, where small-x partons from the Au nucleus are probed, and an enhancement was seen in the backward (Au-going) direction. Similar behavior was previously observed for inclusive charged hadrons and open heavy flavor in d + Au collisions [14,15], potentially indicating similar particle production and modification mechanisms.

The rapidity dependence y of particle production in asymmetric collisions with a smaller-A projectile and a large-A target, provides a way to investigate both hot and CNM effects. Previous J/ψ meson data in Cu + Au collisions [16] showed that the ratio of forward ($1.2 < y < 2.2$, or Cu-going) to backward ($-2.2 < y < -1.2$, or Au-going) J/ψ modification was comparable in both sign and magnitude to that expected from CNM effects. The ϕ meson is composed of lighter closed flavor ($s\bar{s}$) and its production from 1.0 to 5.0 GeV/c involves a mix of soft and hard processes and would provide a link between heavy flavor and lighter mesons. Comparison of the ϕ meson production in Cu + Au and d + Au systems and to J/ψ production in Cu + Au collisions may shed light on the mixture of HNM and CNM effects on ϕ meson production.

The production of ϕ mesons has already been measured at PHENIX in $p + p$, d + Au, Cu + Cu, and Au + Au at midrapidity [17–19] and in $p + p$ and d + Au at forward and backward rapidities [13,20] over a wide range in p_T. Previous measurements from Au + Au and Cu + Cu collisions [18] in a similar momentum range were found to be consistent with HNM effects and exhibited large flow anisotropies. The STAR Collaboration has also previously measured ϕ meson production at midrapidity in Cu + Cu and Au + Au collisions [21,22]. ϕ meson production has also been measured by the ALICE Collaboration at large rapidity in $p + p$ and p + Pb collisions [23] and at midrapidity in Pb + Pb collisions [24].

In this paper, the production of ϕ mesons is determined at forward and backward rapidities via dimuons reconstructed in the PHENIX muon spectrometers in Cu + Au collisions at $\sqrt{s_{NN}} = 200$ GeV recorded in 2012. The particle multiplicity at these rapidities in heavy-ion collisions results in large combinatorial backgrounds and produces a challenging environment for ϕ meson measurements. Previous measurements were thus limited to smaller collision species. A procedure for removing the background is detailed and a measurement of the ϕ meson nuclear-modification factor R_{CuAu} in Cu + Au collisions at forward and backward rapidities is presented versus y, p_T, and the number of participating nucleons.

II. EXPERIMENTAL SETUP

The PHENIX detector is described in detail in Ref. [25], and a schematic of the 2012 setup is shown in Fig. 1. This analysis uses the dimuon decay channel of the ϕ meson. The detectors relevant for this measurement are forward and backward muon spectrometers [26], the two beam-beam counters (BBCs) [27], the silicon vertex tracker (VTX) [28], and the forward silicon vertex detector (FVTX) [29].

This study used minimum bias (MB) events triggered by the BBCs. The BBCs comprise two arrays of 64 Čerenkov counters covering the pseudorapidity range $3.1 < |\eta| < 3.9$. The MB trigger required two or more counters firing on each side and a z-vertex selection around the nominal center of the detector acceptance [16]. The MB trigger fired on $93 \pm 3\%$ of the 5.2 ± 0.2-b total inelastic Cu + Au cross section. In this case, the z vertex was measured by the BBCs with a resolution of $\sigma_z \approx 0.5$–2.0 cm, depending on the event multiplicity.

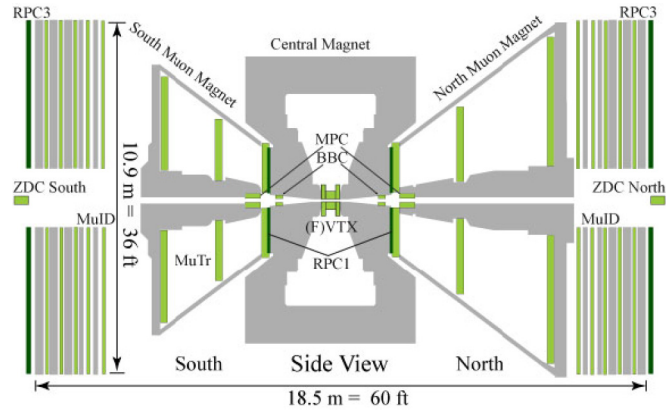

FIG. 1. The 2012 setup of the PHENIX detector.

The collision point is determined in x, y, and z by the two vertex detectors, VTX and FVTX, with a resolution of better than 100 μm. The VTX and FVTX detectors were installed in 2011 and 2012 to provide precise particle vertexing and tracking in the central and forward/backward rapidities. Covering approximately the same rapidity range as the existing muon spectrometers, the FVTX is composed of two end caps, each with four stations that are perpendicular to the beamline and composed of silicon ministrip sensors that have a 75-μm pitch in the radial direction and lengths in the ϕ direction varying from 3.4 to 11.5 mm. The VTX, which surrounds the collision region at PHENIX, comprises four layers of silicon sensors. The inner two layers and outer two layers are composed of 30 pixel ladders and 44 stripixel ladders, respectively.

The muon system is separated into the north and south muon arms. Each arm comprises four subcomponents: an absorber material, a magnet, a muon tracker (MuTr), and a muon identifier (MuID). Initially, the absorbers were composed of 19 cm copper and 60 cm iron, but an additional 36.2 cm of stainless steel was added in 2010 to help decrease the hadronic background. Following the absorber in each muon arm is the MuTr, which comprises three sets of cathode strip chambers in a radial magnetic field with an integrated bending power of 0.8 T m. The final component is the MuID, which comprises five alternating steel absorbers and Iarocci tubes to further reduce the number of punch-through hadrons that can be mistakenly identified as muons. The back plates of the magnets provide the first absorber layer for the MuID systems. The back plate of the south muon magnet is 10 cm shorter than the back plate of the north muon magnet, resulting in less total absorber material in the south arm than the north arm and thus a slightly different momentum acceptance. The muon spectrometers cover the pseudorapidity range $1.2 < |\eta| < 2.2$ over the full azimuth. Muon candidates are identified by reconstructed tracks in the MuTr matched to MuID tracks, where at least one of the tracks from a pair of muon candidates in the same event penetrates through to the last MuID plane.

TABLE I. Quality cuts for ϕ meson signal extraction in Cu + Au collisions.

Variable	Au-going	Cu-going	Meaning
$\lvert z_{\rm vtx}\rvert$ (cm)	<10	<10	Collision vertex along the beam direction as measured by the BBCs
$pDG0$ (GeV/c cm)	<90	<50	Track momentum times the spatial difference between the MuTr track and MuID track at the first MuID layer
$pDDG0$ (GeV/c rad)	<30	<45	Track momentum times the slope difference between the MuTr track and MuID track at the first MuID layer
Track χ^2	<5	<10	χ^2/NDF of the μ track
Lastgap	One track $\geqslant 2$ Other track $\geqslant 4$	One track $\geqslant 2$ Other track $\geqslant 4$	Last MuID plane that the μ track penetrated
nidhits	$>(2\times$lastgap $-1)$	$>(2\times$lastgap $-1)$	Number of hits in the MuID, out of the maximum 10
ntrhits	>11	>10	Number of hits in the MuTr, out of the maximum 16
$\chi^2_{\rm vtx}$	<4	<7	χ^2/NDF of the dimuon track with the vertex
Dimuon p_T(GeV/c)	1–5	1–5	Transverse momentum of the dimuon pair
$\lvert p_z\rvert$ (GeV/c)	>2.4	>2.5	Momentum of the μ along the beam axis

The minimum momentum needed for a muon to reach the last MuID plane is $\sim$3 GeV/c.

III. DATA ANALYSIS

A. Dataset and quality cuts

In this analysis, ϕ meson candidates are selected from two reconstructed muons in the RHIC Cu + Au dataset from 2012. The ϕ meson invariant yields are then measured and used to calculate the nuclear modification factor $R_{\rm CuAu}$, which is compared to results from other systems. For this analysis, 4.73×10^9 ($\mathcal{L} = 0.97$ nb^{-1}) sampled MB events were used within $\pm$10-cm z vertex and 0%–93% centrality. The total inelastic cross section for Cu + Au collisions at 200 GeV was estimated by a Glauber simulation to be 5.2 ± 0.2 b.

A set of quality assurance cuts is applied to the data to select good muon candidates and improve the signal-to-background ratio. These cuts are summarized in Table I. The collision z vertex is required to be within $\pm$10 cm of the center of the interaction region along the beam direction, as measured with the BBCs. The MuTr tracks are required to match the MuID tracks at the first MuID layer in both position and angle. In addition, only dimuon candidates in which at least one track penetrated to the final MuID layer are selected. Furthermore, the track is required to have greater than a minimum number of possible hits in the MuTr and MuID, and a maximum allowed χ^2 is applied to both the track and vertex determination. There is a minimum allowed single muon momentum along the beam axis, p_z, which is reconstructed and energy loss corrected at the collision vertex. Finally, this analysis is restricted to the dimuon p_T range of 1–5 GeV/c. This limitation is attributable to the large backgrounds and small acceptance at low p_T and small statistics at high p_T, preventing signal extraction of the ϕ meson. The events are sorted into centrality classes using the combined charge from both BBCs [16]. The number of binary collisions $N_{\rm coll}$ and number of participating nucleons $N_{\rm part}$ are extracted from a Glauber simulation [16].

B. Background subtraction

The PHENIX muon spectrometers have a small acceptance for ϕ mesons. Going from the most peripheral centrality bin, 40%–93%, to the most central bin, 0%–20%, the signal-to-background ratio decreases from 0.28 to 0.067 in the Cu-going direction ($1.2 < y < 2.2$) and from 0.37 to 0.090 in the Au-going direction ($-2.2 < y < -1.2$). Owing to the very low signal-to-background ratio, particularly in the most central events, the background subtraction is of crucial importance. Accordingly, several different background subtraction methods were explored and compared.

The invariant mass distribution is formed by combining muon candidate tracks of opposite charge. This unlike-sign invariant mass spectrum contains the ϕ, ρ, and ω mesons, as well as both uncorrelated and correlated backgrounds. The uncorrelated backgrounds come from random combinatorial associations of muon candidates, while the correlated backgrounds arise from open charm decay (e.g., $D\bar{D}$ where both decay semileptonically to muons), open beauty decay, η meson and ω meson Dalitz decays, and the Drell-Yan process. These correlated backgrounds are described in Sec. III C. The uncorrelated combinatorial background is accounted for via two methods: (1) like-sign dimuons and (2) event mixing.

First, the uncorrelated combinatorial background is estimated through the like-sign background subtraction technique, which is generally associated with the assumption that the like-sign dimuon pairs come purely from combinatorial processes without any correlation between muons. It follows that the like-sign distribution can be subtracted from the unlike-sign distribution according to the relationship described in Eq. (1),

$$N_{+-} = \mathrm{FG}_{+-} - \mathrm{FG}_{\pm\pm}, \tag{1}$$

where N_{+-} is the uncorrelated background subtracted signal and FG_{+-} and $\mathrm{FG}_{\pm\pm}$ are the unlike-sign and like-sign dimuon pairs, respectively, corresponding to pairs formed within the same event. The like-sign distribution $\mathrm{FG}_{\pm\pm}$ is normalized to a quantity that is more precise and not sensitive to differences in the detector acceptance between like-sign and unlike-sign pairs. This background normalization is described in Eq. (2) [30],

$$\mathrm{FG}_{\pm\pm} = (\mathrm{FG}_{++} + \mathrm{FG}_{--}) \frac{2\sqrt{\int \mathrm{FG}_{++} dm \int \mathrm{FG}_{--} dm}}{\int (\mathrm{FG}_{++} + \mathrm{FG}_{--}) dm}, \tag{2}$$

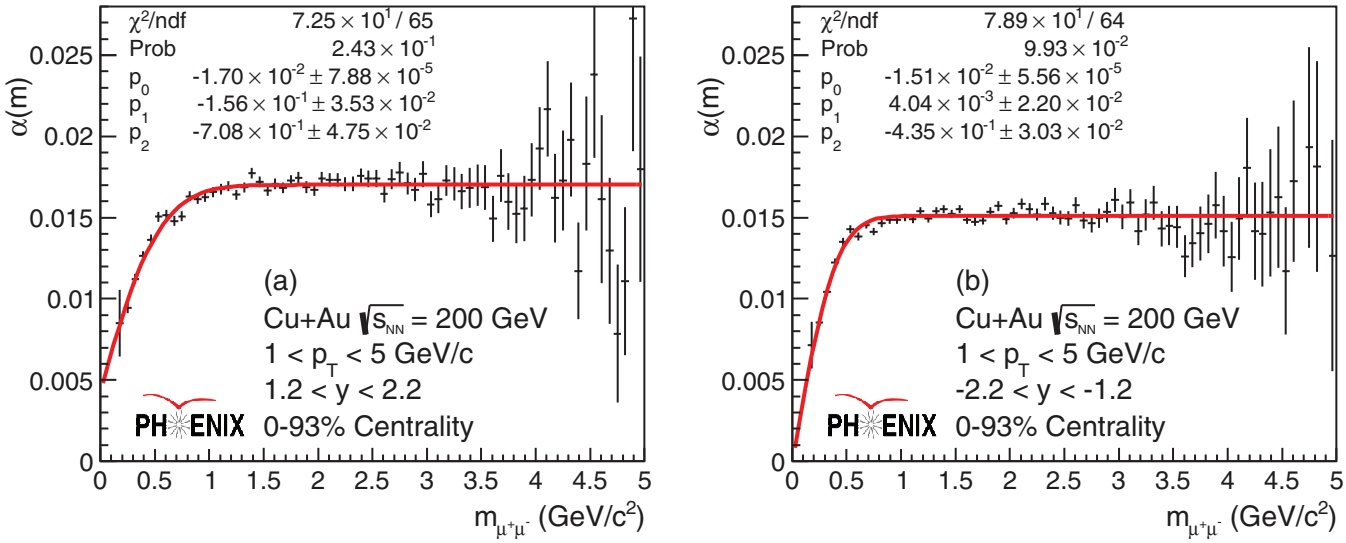

FIG. 2. The event-mixing normalization factor α versus mass. This factor shows a dependence on mass, particularly in the low-mass region. The error function, which was used to fit α, can also be seen in the plot along with the fit parameters and goodness of fit.

where m is the dimuon invariant mass and the integration is carried out in the range $0.2 < m < 5.0\ \mathrm{GeV}/c^2$.

In parallel to the like-sign technique, the uncorrelated background is also estimated through the event-mixing technique. In the standard event-mixing method, muons from different events are randomly associated to produce a background distribution of uncorrelated dimuon pairs. Events were mixed with partners from within the same 2%-centrality and 1-cm z-vertex bins to minimize the systematic uncertainties. The mixed-event background distributions (BG) were generated with about 8 times higher statistics than the actual background and then normalized to match the same-event foreground (FG). The normalization factor also accounts for slightly different multiplicities from mixing of slightly different events. Although a mass-dependent technique was developed for this analysis, a standard event-mixing technique is described in advance. In previous PHENIX analyses, the normalization factor α was calculated as described in Eq. (3),

$$\alpha = \sqrt{\frac{\int \mathrm{FG}_{++}dm \int \mathrm{FG}_{--}dm}{\int \mathrm{BG}_{++}dm \int \mathrm{BG}_{--}dm}}, \tag{3}$$

where FG_{++} and FG_{--} are the like-sign pairs from the same event and BG_{++} and BG_{--} are the like-sign pairs from mixed events.

After subtracting and fitting the resonances as well as the remaining correlated background, the yields from mixed-event background subtraction are consistent with the yields from

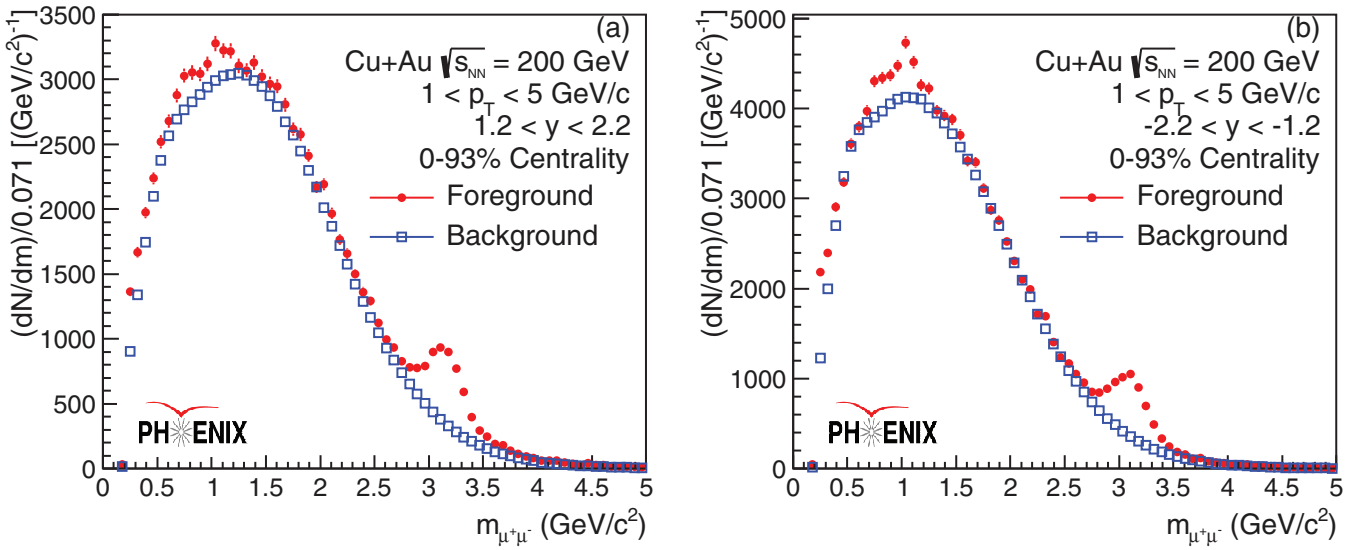

FIG. 3. The unlike-sign spectra and combinatorial background described with event mixing for $1.2 < y < 2.2$ (Cu-going direction) and $-2.2 < y < -1.2$ (Au-going direction). The $\rho + \omega$, ϕ, and J/ψ peaks are clearly visible before background subtraction. The mass bin width is 71 MeV, as marked on the vertical axis.

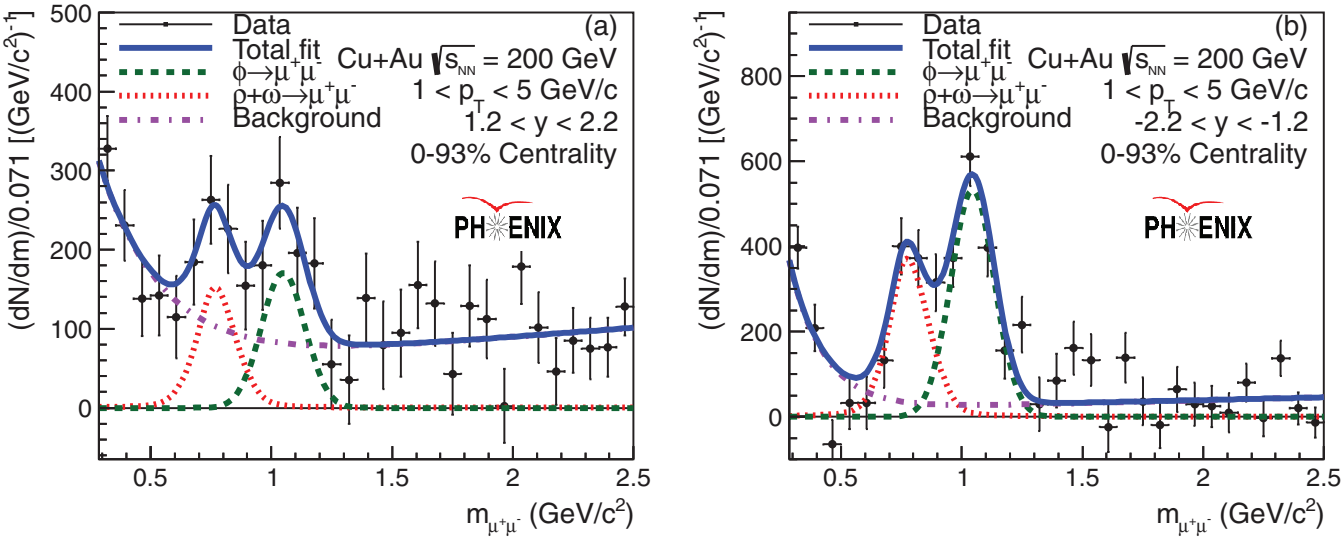

FIG. 4. The dimuon mass spectra for $1.2 < y < 2.2$ (Cu-going direction) and $-2.2 < y < -1.2$ (Au-going direction) after subtracting mixed events and fitting the ϕ and $\rho + \omega$ peaks and the remaining correlated background. The mass bin width is 71 MeV, as marked on the vertical axis.

the like-sign technique within statistical uncertainties. The event-mixing technique is used in this analysis owing to the statistical limitations of the like-sign technique. The differences between the like-sign and event-mixing techniques are used to determine one component of the systematic uncertainty on the yield, as described later in Sec. III F.

In this method, each term in the square root of Eq. (3) was integrated over all mass, introducing a mass-independent normalization factor [16,31]. Dimuons from same events are less likely to be reconstructed in close proximity to each other than those in mixed events, resulting in a larger relative number of mixed-event dimuons at low mass, where the opening angle is small, than at higher mass. Therefore, the normalization factor, which is simply a ratio of the like-sign same-event dimuons to like-sign mixed-event dimuons, drops at lower masses. Because this normalization factor depends on mass, particularly in the ϕ meson region, it became necessary to introduce a mass-dependent normalization, as described in Eq. (4), rather than the more commonly used mass-integrated normalization from Eq. (3):

$$\alpha(m) = \sqrt{\frac{\mathrm{FG}_{++}(m)\mathrm{FG}_{--}(m)}{\mathrm{BG}_{++}(m)\mathrm{BG}_{--}(m)}}. \tag{4}$$

This mass-dependent normalization factor is then fit as a function of mass, and the fit function—rather than the integrated normalization factor—is multiplied to the unlike-sign mixed-event background to get the normalized background spectrum $\mathrm{BG}_{+-}^{\mathrm{normalized}}$,

$$\mathrm{BG}_{+-}^{\mathrm{normalized}}(m) = \alpha(m) \times \mathrm{BG}_{+-}(m). \tag{5}$$

Several fitting functions were tested, including a polynomial and an error function. The error function, which is used in the final analysis, is described in Eq. (6), where $g(m)$ is the error function and p_0, p_1, and p_2 are free parameters of the fit. A plot of the normalization factor as a function of mass fit with an error function is shown in Fig. 2:

$$g(m) = p_0 \times \mathrm{Erf}\left(\frac{m - p_1}{p_2}\right). \tag{6}$$

The application of event mixing to describe and subtract backgrounds in the ϕ meson mass region is shown in Fig. 3, where the open squares represent the mixed-event background and the closed circles are the unlike-sign spectrum. Before background subtraction, the $\rho + \omega$, ϕ and J/ψ peaks are clearly seen.

C. Signal extraction and correlated background

After the mixed-event background subtraction, there is still some correlated background remaining. In previous PHENIX analyses, it was shown that heavy flavor (charm and beauty) contributions were negligible in the ϕ meson mass region for $p + p$ and $d + \mathrm{Au}$ collisions at 200 GeV [13,20]. Simulation studies showed that η meson Dalitz decays are one possible contributor to the correlated background. The correlated background is well described by the function in Eq. (7),

$$f(m) = \exp(am) + b + cm, \tag{7}$$

TABLE II. Systematic uncertainties included in the invariant yield calculations.

Type	Origin	Value (%)
A	Signal extraction	2–31
B	MuID efficiency	2
B	MuTr efficiency	2
B	$A\varepsilon_{\mathrm{rec}}$	13
B	ϕ candidate selection	3
B	Like-sign background subtraction	5
C	MB trigger	3

TABLE III. Systematic uncertainties included in the nuclear-modification factor calculations.

Type	Origin	Value (%)
A	Signal extraction	2–31
A	$p+p$ reference (integrated centrality only)	5–13
B	MuID efficiency	4
B	MuTr efficiency	2
B	$A\varepsilon_{\rm rec}$	13
B	ϕ candidate selection	3
B	Like-sign background subtraction	5
B	$N_{\rm coll}$ (centrality bins only)	5–10
C	MB trigger	10
C	$N_{\rm coll}$ (integrated centrality only)	5
C	$p+p$ reference (centrality bins only)	11

where a, b, and c are free parameters of the fit $f(m)$. Accordingly, the correlated background in real data are also fit with the function described in Eq. (7), as shown in Fig. 4, where the mass distribution after mixed-event background subtraction is shown. Several other fit functions and fit ranges were tested and used to estimate a systematic uncertainty.

The ϕ and ω meson signals are each described by a Gaussian and the signal from the ρ meson by a Breit-Wigner distribution, as shown in Fig. 4, along with the correlated background description. The ϕ meson mass resolution is $\sim$90 MeV/c^2. The PHENIX muon arms are not able to resolve the ρ and ω peaks separately, so a combined fit is made. All fit parameters are constrained but allowed to vary, except the ratio of the yield of ρ mesons to that of $\rho+\omega$, which is set as a constant based on the expected ratio between their cross sections and branching ratios. The data are binned as a function of p_T, y, and centrality over the range $1 < p_T < 5$ GeV/c, $1.2 < |y| < 2.2$, and 0%–93% centrality.

D. Detector acceptance and reconstruction efficiency

The product of detector acceptance and reconstruction efficiency, $A\varepsilon_{\rm rec}$, of dimuon decays of ϕ mesons is determined by the full event reconstruction of the ϕ meson signal obtained from PYTHIA6.42 [32], run through a full GEANT3 [33] simulation of the 2012 PHENIX detector setup, and embedded in the MB real-data background. The embedded simulated events are then reconstructed in the same manner as data with the same cuts applied as in the real data analysis. The background subtraction and signal extraction are also handled in the exact same manner as in real data. The $A\varepsilon_{\rm rec}$ is then calculated as the number of reconstructed ϕ meson candidates divided by the number of ϕ mesons generated in PYTHIA, both within an appropriate kinematic bin. As previously mentioned, the south arm has a smaller amount of absorber material, causing a larger acceptance in the south arm (Au-going direction) than in the north arm (Cu-going direction). In addition, the $A\varepsilon_{\rm rec}$ has a centrality and p_T dependence. Specifically, for the lower-p_T bin (1–2.5 GeV/c), $A\varepsilon_{\rm rec} = 1.21\times10^{-3}$ in the Cu-going direction and 1.86×10^{-3} in the Au-going direction, while for the higher-p_T bin (2.5–5 GeV/c), $A\varepsilon_{\rm rec} = 1.69\times10^{-2}$ in the Cu-going direction and 1.81×10^{-2} in the Au-going direction. The centrality dependence is not as strong, with the values going from $A\varepsilon_{\rm rec} = 2.23\times10^{-3}$ in the Cu-going direction and 2.37×10^{-3} in the Au-going direction at 0%–20% centrality to $A\varepsilon_{\rm rec} = 2.41\times10^{-3}$ in the Cu-going direction and 3.83×10^{-3} in the Au-going direction at 40%–93% centrality.

E. Invariant yields and nuclear-modification factors

The invariant yield is calculated according to the relation

$$\mathrm{BR}\frac{d^2N}{dydp_T} = \frac{1}{\Delta y\Delta p_T}\frac{N}{A\varepsilon_{\rm rec}N_{\rm evt}}, \tag{8}$$

where BR is the branching ratio to dimuons ($\mathrm{BR}(\phi\to\mu^+\mu^-) = (2.89\pm0.19)\times10^{-4}$ [34]), $N_{\rm evt}$ is the number of sampled MB events within the relevant centrality selection ($N_{\rm evt} = 4.73\times10^9$ for the 0%–93% selection), N is the number of observed ϕ mesons, and Δy and Δp_T are the bin widths in y and p_T, respectively. To evaluate the nuclear-matter effects on ϕ meson production in Cu + Au collisions, the ϕ meson yields in Cu + Au collisions are compared to those measured in $p+p$ collisions at the same energy after scaling by the number of nucleon-nucleon collisions in the Cu + Au system, $N_{\rm coll}$. This ratio is called the nuclear-modification factor $R_{\rm CuAu}$ and is defined as

$$R_{\rm CuAu} = \frac{\frac{d^2N_{\rm CuAu}}{dydp_T}}{N_{\rm coll}\times\frac{d^2N_{pp}}{dydp_T}}. \tag{9}$$

The $p+p$ reference data used in the $R_{\rm CuAu}$ are from Ref. [20]. Because the rapidity and p_T binning in the Cu + Au analysis differs from that in the $p+p$ analysis, the $p+p$ invariant yields were remeasured using the same binning as the Cu + Au yields and in a manner similar to that in Ref. [20]. The sampled luminosity of the $p+p$ data used in this analysis corresponds to $\mathcal{L} = 14.1$ pb^{-1} [20].

TABLE IV. Invariant yield as a function of centrality for $1 < p_T < 5$ GeV/c and $1.2 < |y| < 2.2$. The first value represents the statistical and type A systematic uncertainties, while the second is the systematic uncertainty of type B. An additional ±3% type C global systematic uncertainty also applies to the yields. The last column summarizes the forward/backward ratio shown in Fig. 11. The forward/backward ratio has no type C systematic uncertainty.

Centrality bin (%)	$\langle N_{\rm part}\rangle$	$\mathrm{BR}\frac{dN}{dy}$ (Cu-going)	$\mathrm{BR}\frac{dN}{dy}$ (Au-going)	Forward/backward ratio
0–20	154.8 ± 4.1	$(7.3\pm7.5\pm1.1)\times10^{-5}$	$(3.4\pm1.0\pm0.5)\times10^{-4}$	$0.2^{+0.3}_{-0.2}\pm<0.1$
20–40	80.4 ± 3.3	$(1.2\pm0.3\pm0.2)\times10^{-4}$	$(1.2\pm0.3\pm0.2)\times10^{-4}$	$1.0^{+0.4}_{-0.3}\pm0.1$
40–93	19.5 ± 0.5	$(1.5\pm0.6\pm0.2)\times10^{-5}$	$(2.7\pm0.7\pm0.4)\times10^{-5}$	$0.6^{+0.4}_{-0.3}\pm0.1$

TABLE V. Invariant yield as a function of p_T for 0%–93% centrality and $1.2 < |y| < 2.2$. The first error represents the statistical and type A systematic uncertainties, while the second is the systematic uncertainty of type B. An additional ±5.8% type C global systematic uncertainty also applies.

$p_T^{\min}$ (GeV/c)	$p_T^{\max}$ (GeV/c)	BR $\frac{d^2N}{dydp_T}$ (Cu-going) $(\text{GeV}/c)^{-1}$	BR $\frac{d^2N}{dydp_T}$ (Au-going) $(\text{GeV}/c)^{-1}$
1.0	2.5	$(2.7 \pm 0.8 \pm 0.4) \times 10^{-5}$	$(5.5 \pm 0.9 \pm 0.8) \times 10^{-5}$
2.5	5.0	$(1.8 \pm 1.0 \pm 0.3) \times 10^{-7}$	$(4.1 \pm 1.0 \pm 0.6) \times 10^{-7}$

F. Systematic uncertainties

The systematic uncertainties associated with this measurement are categorized as type A, type B or type C. Type A refers to point-to-point uncorrelated uncertainties that allow the data points to move independently with respect to one another. They are added in quadrature with the statistical uncertainties and represented on the plots as an error bar. Type B uncertainties are correlated point-to-point, which means the points move coherently. All sources of type B uncertainty are added in quadrature and displayed as boxes around the data points. Finally, type C refers to the global uncertainties which allow the data points to move together by an identical multiplicative factor. The type C uncertainties are given in the legends of the plots.

Several systematic uncertainties are evaluated for this analysis. For the signal extraction uncertainty, different fits and parameters are tested for the background normalization factor, the correlated background, the $\rho + \omega$ signal, and the ϕ meson signal. This is done separately for each kinematic bin, and a 2%–31% systematic uncertainty is assigned, with the largest uncertainty on yields extracted from the most central events. This is because the high multiplicity in central collisions results in large combinatorial backgrounds and a very small signal-to-background ratio. It is important to note here that the signal extraction uncertainty was primarily dominated by the fluctuations in the correlated background. The $p + p$ reference uncertainty comes from the uncertainty on the ϕ yields in the $p + p$ reference [20]. There is a 4% systematic uncertainty from the MuID efficiency and a 2% uncertainty from the MuTr efficiency in $p + p$ collisions [20]. In Cu + Au collisions, the MuTr efficiency uncertainty remains the same, while the MuID efficiency uncertainty drops down to 2% [16]. For the $A\varepsilon_{\text{rec}}$ uncertainty, the p_T and y distributions in PYTHIA are changed to match the slope of the distributions in real data and allowed to vary over the range of the error bars in data, yielding a 13% systematic uncertainty. Real data and simulation inconsistencies in each of the muon identification cuts listed in Table I are also evaluated. They can affect the yields by 3%, which is assigned as a systematic uncertainty on the ϕ meson candidate selection. The like-sign background subtraction uncertainty of 5% comes from differences in the yields when using the like-sign method or the event mixing method. The N_{coll} uncertainty of 5%–10% arises from the fact that N_{coll} carries a statistical uncertainty itself. Finally, the MB trigger efficiency uncertainty was 10% in the $p + p$ reference [20] and 3% in Cu + Au collisions [16]. All of these systematic uncertainties are tabulated in Tables II and III.

TABLE VI. Invariant yield as a function of rapidity for 0%–93% centrality and $1 < p_T < 5$ GeV/c. The first error represents the statistical and type A systematic uncertainties, while the second is the systematic uncertainty of type B. An additional ±5.8% type C global systematic uncertainty also applies.

$\lvert y\rvert^{\min}$	$\lvert y\rvert^{\max}$	BR $\frac{dN}{dy}$ (Cu-going)	BR $\frac{dN}{dy}$ (Au-going)
1.8	2.2	$(6.4 \pm 3.1 \pm 0.9) \times 10^{-5}$	$(1.1 \pm 0.2 \pm 0.2) \times 10^{-4}$
1.2	1.8	$(5.3 \pm 2.3 \pm 0.8) \times 10^{-5}$	$(1.1 \pm 0.3 \pm 0.2) \times 10^{-4}$

IV. RESULTS

The invariant yields for $1 < p_T < 5$ GeV/c ϕ mesons are calculated as a function of centrality, y, and p_T, as described in Eq. (8). The results are summarized in Tables IV–VI. Similarly, the nuclear modification factors are formed from the invariant yields using Eq. (9) and tabulated in Tables VII–IX.

Figure 5 shows the invariant yield as a function of the number of participating nucleons N_{part}. In Fig. 6, the dependence of the invariant yield on transverse momentum p_T is shown. The invariant yield as a function of rapidity is plotted in Fig. 7. More ϕ mesons are produced in the Au-going direction ($-2.2 < y < -1.2$) than in the Cu-going direction ($1.2 < y < 2.2$). This may be explained by the larger multiplicity in the Au-going direction coupled with a mixture of both HNM and CNM effects.

Although the invariant yields are interesting on their own, the nuclear modification factor is studied to evaluate the effects of hot and cold nuclear matter on ϕ meson production in Cu + Au collisions at $\sqrt{s_{NN}} = 200$ GeV.

The nuclear-modification factor as a function of N_{part} is shown in Fig. 8. There is a dependence of R_{CuAu} on both centrality and rapidity. In the Au-going direction, the R_{CuAu} is greater than unity for all centralities. The rapidity dependence is similar to the trend observed by PHENIX for $\phi \to \mu^+\mu^-$ in

TABLE VII. Nuclear modification factors as a function of centrality for $1 < p_T < 5$ GeV/c and $1.2 < |y| < 2.2$. The first error represents the statistical and type A systematic uncertainties, while the second is the systematic uncertainty of type B. An additional ±15% type C global systematic uncertainty also applies.

Centrality bin (%)	$\langle N_{\text{coll}} \rangle$	R_{CuAu} (Cu-going)	R_{CuAu} (Au-going)
0–20	313.8 ± 28.4	$0.4 \pm 0.4 \pm 0.1$	$1.7 \pm 0.5 \pm 0.3$
20–40	129.3 ± 12.4	$1.4 \pm 0.4 \pm 0.3$	$1.4 \pm 0.3 \pm 0.3$
40–93	21.6 ± 1.0	$1.1 \pm 0.5 \pm 0.2$	$1.9 \pm 0.5 \pm 0.3$

TABLE VIII. Nuclear modification factors as a function of p_T for 0%–93% centrality and $1.2 < |y| < 2.2$. The first error represents the statistical and type A systematic uncertainties, while the second is the systematic uncertainty of type B. An additional ±11% type C global systematic uncertainty also applies.

$p_T^{\min}$ (GeV/c)	$p_T^{\max}$ (GeV/c)	R_{CuAu} (Cu-going)	R_{CuAu} (Au-going)
1.0	2.5	$1.1 \pm 0.4 \pm 0.2$	$2.3 \pm 0.4 \pm 0.4$
2.5	5.0	$0.6 \pm 0.4 \pm 0.1$	$1.4 \pm 0.3 \pm 0.2$

d + Au collisions [13], as well as measurements made by the ALICE Collaboration at large rapidity in p + Pb collisions at 5.02 TeV at the Large Hadron Collider [23], where an enhancement was observed in the Pb-going direction, while the p-going direction was either suppressed or consistent with unity depending on the p_T range.

To further understand the relative roles of different nuclear-matter effects in this collision system, the transverse momentum dependence of the nuclear-modification factor is shown in Fig. 9. The data points are placed at the mean p_T of the bin. Here the nuclear modification is calculated over integrated centrality, but it should be noted that the data are dominated by central collisions. There is an enhancement at low p_T in the Au-going direction. In the Cu-going direction, R_{CuAu} is consistent with unity. The enhancement in the Au-going direction is similar in scale to that observed in the Au-going direction in d + Au collisions [13], indicating similar nuclear modification between the two collision systems.

Figure 10 shows the nuclear-modification factor R_{CuAu} as a function of y for two rapidity regions, $1.2 < |y| < 1.8$ and $1.8 < |y| < 2.2$. The data points are placed at the mean y of the bin. As in Fig. 9, the nuclear-modification factor is inclusive of centrality. The rapidity dependence of R_{CuAu} is similar to the trend observed in previous ϕ meson measurements in d + Au and p + Pb collisions. In particular, ϕ meson production is enhanced in the Au-going direction. None of the Cu-going points show significant suppression given the statistical uncertainties. For comparison, the PHENIX J/ψ meson results in the same Cu + Au dataset from Ref. [16] are also shown in Fig. 10. While the closed charm shows suppression at both forward and backward rapidity for $1.2 < |y| < 2.2$, the closed strangeness is enhanced at backward rapidity. In Cu + Au collisions, the J/ψ meson yield is strongly suppressed in the Au-going direction compared to the ϕ meson yield at the same rapidity. This is similar to the differences previously observed between J/ψ and ϕ meson nuclear modification in d + Au collisions

TABLE IX. Nuclear-modification factors as a function of rapidity for 0%–93% centrality and $1 < p_T < 5$ GeV/c. The first error represents the statistical and type A systematic uncertainties, while the second is the systematic uncertainty of type B. An additional ±11% type C global systematic uncertainty also applies.

$\lvert y\rvert^{\min}$	$\lvert y\rvert^{\max}$	R_{CuAu} (Cu-going)	R_{CuAu} (Au-going)
1.8	2.2	$1.2 \pm 0.6 \pm 0.2$	$2.1 \pm 0.5 \pm 0.3$
1.2	1.8	$0.7 \pm 0.3 \pm 0.1$	$1.4 \pm 0.4 \pm 0.2$

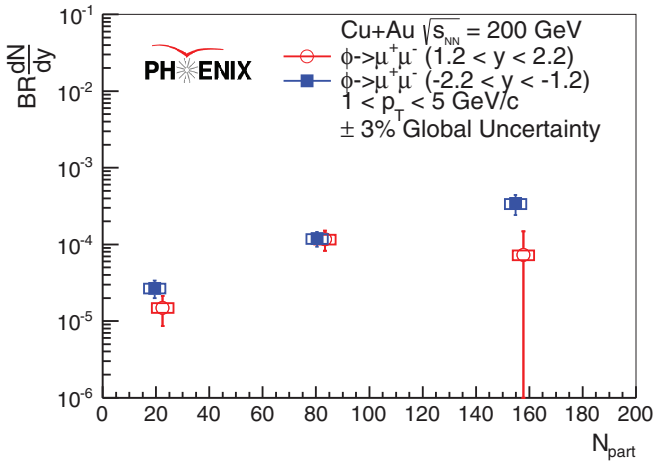

FIG. 5. Invariant yield as a function of the number of participating nucleons for $1.2 < |y| < 2.2$ and $1 < p_T < 5$ GeV/c. The centrality bins are 0%–20%, 20%–40%, and 40%–93%, and the data points are placed at the mean N_{part} calculated from a Glauber simulation. The data points for the Cu-going direction, $1.2 < y < 2.2$, are shifted along the x axis to $N_{\mathrm{part}} + 3$ to make the points visible, while the Au-going direction, $-2.2 < y < -1.2$, remains unshifted. The values are shown in Table IV.

[13]. These differences could be attributed to a larger J/ψ breakup cross section, effects in the higher-energy-density backward-rapidity region, or changes between soft and hard production mechanisms between the two mesons.

The forward and backward differences can be quantified by the ratio of the yield values for the forward rapidity (Cu-going direction) to the backward rapidity (Au-going direction). Figure 11 shows the forward/backward ratio as a function of participating nucleons for $1.2 < |y| < 2.2$ and

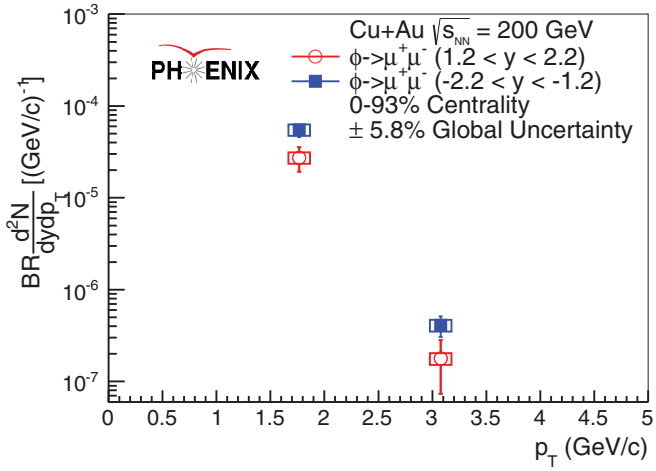

FIG. 6. Invariant yield as a function of transverse momentum for $1.2 < |y| < 2.2$ and 0%–93% centrality. The p_T bins are $1 < p_T \leqslant 2.5$ and $2.5 < p_T < 5$ GeV/c, and the data points are placed at the mean p_T of the bin. The Cu-going direction corresponds to the forward rapidity, $1.2 < y < 2.2$, while the Au-going direction corresponds to the backward rapidity, $-2.2 < y < -1.2$. The values are shown in Table V.

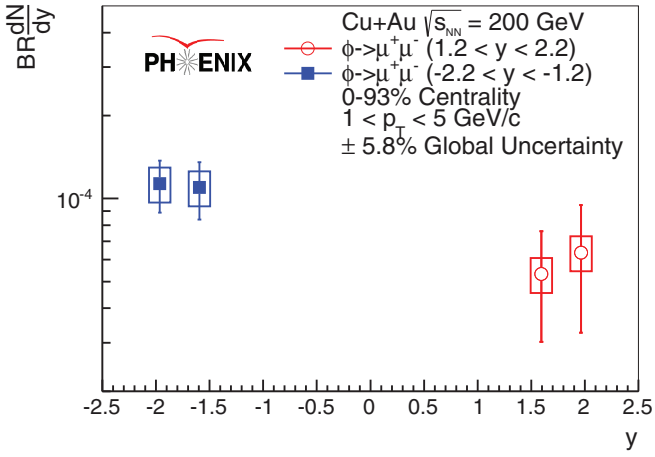

FIG. 7. Invariant yield as a function of rapidity for $1 < p_T < 5$ GeV/c and 0%–93% centrality. The rapidity bins are $1.2 < |y| < 1.8$ and $1.8 < |y| < 2.2$ and the data points are placed at the mean y of the bin. The Cu-going direction covers the region $1.2 < y < 2.2$, while the Au-going direction covers the region $-2.2 < y < -1.2$. The values are shown in Table VI.

$1 < p_T < 5$ GeV/c. The type C and type B systematic uncertainties, except for the $A\varepsilon_{\rm rec}$ uncertainty, cancel when taking this ratio. The remaining systematic uncertainties are the type A signal extraction uncertainty and the type-B $A\varepsilon_{\rm rec}$ uncertainty. The difference in suppression between the forward and backward rapidity is more noticeable in the most central collisions, 0%–20%. In this centrality bin, the probability of observing the forward/backward ratio greater than or equal to unity was found to be p value $= 1.2\%$, corresponding to

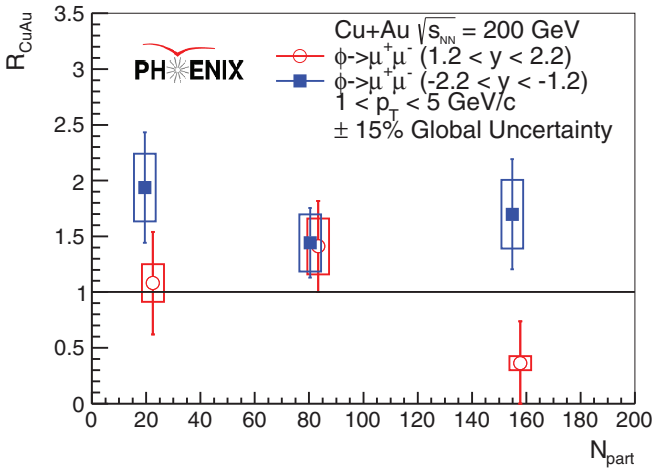

FIG. 8. The nuclear-modification factor $R_{\rm CuAu}$ as a function of the number of participating nucleons for $1.2 < |y| < 2.2$ and $1 < p_T < 5$ GeV/c. The centrality bins are 0%–20%, 20%–40%, and 40%–93%, and the data points are placed at the mean $N_{\rm part}$ calculated from a Glauber simulation. The data points for the Cu-going direction, $1.2 < y < 2.2$, are shifted along the x axis to $N_{\rm part} + 3$ to make the points visible, while the data points for the Au-going direction, $-2.2 < y < -1.2$, remain unshifted. The values are shown in Table VII.

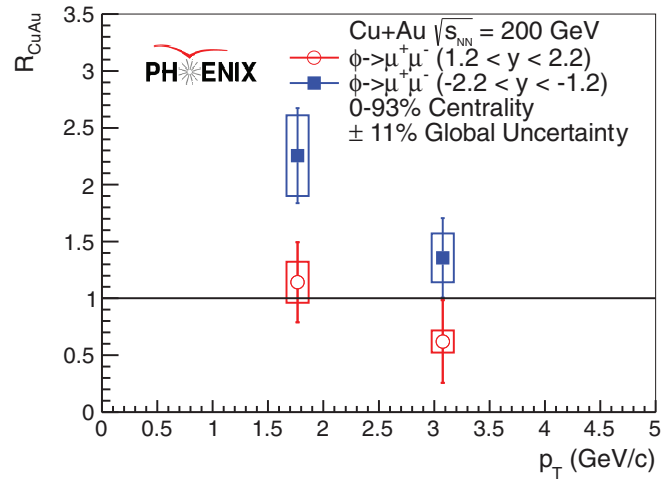

FIG. 9. The nuclear-modification factor $R_{\rm CuAu}$ as a function of transverse momentum for $1.2 < |y| < 2.2$ and 0%–93% centrality. The p_T bins are $1 < p_T \leqslant 2.5$ and $2.5 < p_T < 5$ GeV/c, and the data points are placed at the mean p_T of the bin. The Cu-going direction corresponds to the forward rapidity, $1.2 < y < 2.2$, while the Au-going direction corresponds to the backward rapidity, $-2.2 < y < -1.2$. The values are shown in Table VIII.

a statistical significance of 2.3σ. The particle multiplicity for central collisions should be about 20% higher in the Au-going direction than in the Cu-going direction [35]; however, the much smaller ratio observed may indicate that increased recombination effects or additional thermal strangeness production may also occur at higher energy density. In central collisions, the forward/backward ratio in ϕ production ($\sim$0.2)

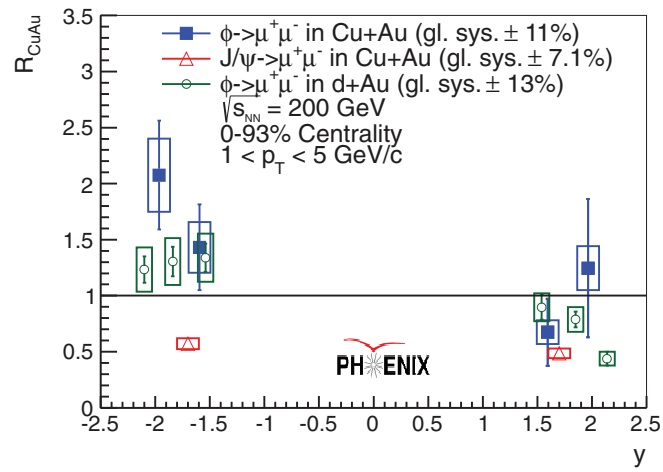

FIG. 10. The nuclear-modification factor $R_{\rm CuAu}$ as a function of rapidity for $1 < p_T < 5$ GeV/c and 0%–93% centrality. The rapidity bins are $1.2 < |y| < 1.8$ and $1.8 < |y| < 2.2$ and the data points are placed at the mean y of the bin. The values are shown in Table IX. Also included are previous PHENIX results for ϕ mesons in d + Au collisions [13], represented by open circles, and J/ψ mesons in Cu + Au collisions [16], represented by open triangles. Positive rapidity, $1.2 < y < 2.2$, corresponds to the Cu-going and d-going directions, while negative rapidity, $-2.2 < y < -1.2$, is the Au-going direction.

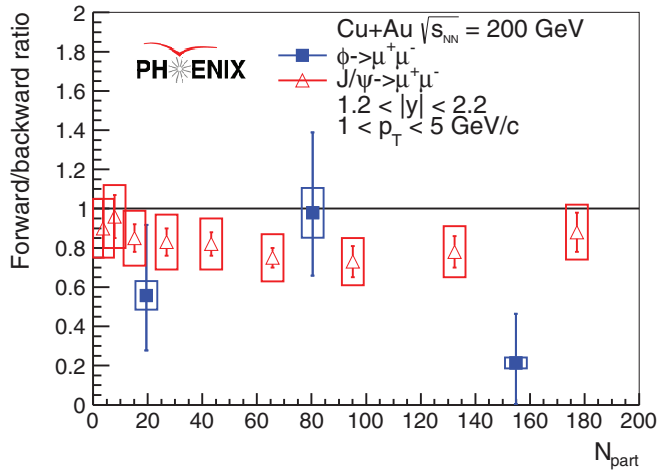

FIG. 11. The forward/backward ratio as a function of the number of participating nucleons for $1 < p_T < 5$ GeV/c and $1.2 < |y| < 2.2$. The values are shown in Table IV. The Cu-going direction covers positive rapidity, $1.2 < y < 2.2$, while the Au-going direction covers negative rapidity, $-2.2 < y < -1.2$.

is smaller than that in J/ψ production ($\sim$0.8) in Cu + Au collisions [16].

V. SUMMARY

In summary, ϕ meson production and its nuclear modification have been measured in Cu + Au collisions at $\sqrt{s_{NN}} =$ 200 GeV for $1.2 < |y| < 2.2$ and $1.0 < p_T < 5.0$ GeV/c via the dimuon decay channel. This first measurement of ϕ meson production and its nuclear modification in a heavy-ion system at forward/backward rapidity at RHIC extends measurements of ϕ from smaller systems, $p + p$ and $d +$ Au, in the forward and backward rapidity. The invariant yields and nuclear-modification factors have been presented here as a function of $N_{\rm part}$, p_T, and rapidity.

The ϕ meson yields in Cu + Au collisions are found to be generally smaller in the Cu-going direction than in the Au-going direction. This is most pronounced in the most central events, 0%–20%, and at low momentum, 1.0–2.5 GeV/c. In central collisions (0%–20%), the forward/backward ratio is below unity at a confidence level of 99%. It has been shown that these results follow a trend similar to what was seen previously at PHENIX in $d +$ Au at the same rapidity and energy [13], as well as the ALICE measurement in $p +$ Pb collisions at larger rapidity ($-4.46 < y < -2.96$ and $2.03 < y < 3.53$) and higher energy ($\sqrt{s_{NN}} = 5.02$ TeV) [23]. While this agreement could imply a role for CNM effects on ϕ production in Cu + Au collisions, the production of ϕ in heavy-ion collisions for these kinematics is expected to have substantial contributions from HNM effects, which were demonstrated to dominate previous measurements at midrapidity for both Cu + Cu and Au + Au collisions [18]. A competition between CNM and HNM production mechanisms appears relevant for ϕ production at forward rapidity for heavy-ion collisions and a comprehensive description is needed from soft and hard physics models. Although the ϕ meson is sensitive to both CNM and HNM effects, this study was statistically limited, a factor that also affects the precise determination of the systematic uncertainties. A high-statistics measurement and theory calculations are both needed to make conclusions about the various physics processes that might be at play here, including modifications of strangeness production in bulk matter and quark recombination.

ACKNOWLEDGMENTS

We thank the staff of the Collider-Accelerator and Physics Departments at Brookhaven National Laboratory and the staff of the other PHENIX participating institutions for their vital contributions. We acknowledge support from two offices within the Office of Science of the Department of Energy: the Office of Nuclear Physics and the Office of Science Graduate Student Research award program, which is administered by the Oak Ridge Institute for Science and Education, and support from the National Science Foundation, Abilene Christian University Research Council, Research Foundation of SUNY, and Dean of the College of Arts and Sciences, Vanderbilt University (USA); Ministry of Education, Culture, Sports, Science, and Technology and the Japan Society for the Promotion of Science (Japan); Conselho Nacional de Desenvolvimento Científico e Tecnológico and Fundação de Amparo à Pesquisa do Estado de São Paulo (Brazil); Natural Science Foundation of China (People's Republic of China); Croatian Science Foundation and Ministry of Science, Education, and Sports (Croatia); Ministry of Education, Youth and Sports (Czech Republic); Centre National de la Recherche Scientifique, Commissariat à l'Énergie Atomique, and Institut National de Physique Nucléaire et de Physique des Particules (France); Bundesministerium für Bildung und Forschung, Deutscher Akademischer Austausch Dienst, and Alexander von Humboldt Stiftung (Germany); National Science Fund, OTKA, Károly Róbert University College, and the Ch. Simonyi Fund (Hungary); Department of Atomic Energy and Department of Science and Technology (India); Israel Science Foundation (Israel); Basic Science Research Program through NRF of the Ministry of Education (Korea); Physics Department, Lahore University of Management Sciences (Pakistan); Ministry of Education and Science, Russian Academy of Sciences, Federal Agency of Atomic Energy (Russia); VR and Wallenberg Foundation (Sweden); the US Civilian Research and Development Foundation for the Independent States of the Former Soviet Union, the Hungarian American Enterprise Scholarship Fund, and the US-Israel Binational Science Foundation.

[1] I. Arsene *et al.* (BRAHMS Collaboration), Quark gluon plasma and color glass condensate at RHIC? The Perspective from the BRAHMS experiment, Nucl. Phys. A **757**, 1 (2005).

[2] B. B. Back *et al.*, The PHOBOS perspective on discoveries at RHIC, Nucl. Phys. A **757**, 28 (2005).

[3] J. Adams *et al.* (STAR Collaboration), Experimental and theoretical challenges in the search for the quark gluon plasma: The STAR Collaboration's critical assessment of the evidence from RHIC collisions, Nucl. Phys. A **757**, 102 (2005).

[4] K. Adcox *et al.* (PHENIX Collaboration), Formation of dense partonic matter in relativistic nucleus-nucleus collisions at RHIC: Experimental evaluation by the PHENIX Collaboration, Nucl. Phys. A **757**, 184 (2005).

[5] P. Koch, B. Muller, and J. Rafelski, Strangeness in Relativistic Heavy Ion Collisions, Phys. Rep. **142**, 167 (1986).

[6] A. Shor, ϕ Meson Production as a Probe of the Quark Gluon Plasma, Phys. Rev. Lett. **54**, 1122 (1985).

[7] A. Andronic, An overview of the experimental study of quark-gluon matter in high-energy nucleus-nucleus collisions, Proceedings, 26th International Symposium on Lepton Photon Interactions at High Energy (LP13), Int. J. Mod. Phys. A **29**, 1430047 (2014).

[8] C. M. Ko and D. Seibert, What can we learn from a second ϕ meson peak in ultrarelativistic nuclear collisions? Phys. Rev. C **49**, 2198 (1994).

[9] J. J. Heckman, J. Seo, and C. Vafa, Phase structure of a brane/anti-brane system at large N, J. High Energy Phys. 07 (2007) 073.

[10] I. Vitev, Initial state parton broadening and energy loss probed in d+Au at RHIC, Phys. Lett. B **562**, 36 (2003).

[11] J. W. Cronin, Henry J. Frisch, M. J. Shochet, J. P. Boymond, R. Mermod, P. A. Piroue, and R. L. Sumner, Production of Hadrons with Large Transverse Momentum at 200 GeV, 300-GeV, and 400-GeV, High energy physics. Proceedings, 17th International Conference, ICHEP 1974, London, England, July 01-July 10, 1974, Phys. Rev. D **11**, 3105 (1975).

[12] A. Accardi and M. Gyulassy, Cronin effect versus geometrical shadowing in d + Au collisions at RHIC, Phys. Lett. B **586**, 244 (2004).

[13] A. Adare *et al.* (PHENIX Collaboration), ϕ meson production in d + Au collisions at $\sqrt{s_{NN}} = 200$ GeV, Phys. Rev. C **92**, 044909 (2015).

[14] S. S. Adler *et al.* (PHENIX Collaboration), Nuclear Modification Factors for Hadrons at Forward and Backward Rapidities in Deuteron-Gold Collisions at $\sqrt{s_{NN}} = 200$ GeV, Phys. Rev. Lett. **94**, 082302 (2005).

[15] A. Adare *et al.* (PHENIX Collaboration), System-size dependence of open-heavy-flavor production in nucleus-nucleus collisions at $\sqrt{s_{NN}} = 200$ GeV, Phys. Rev. C **90**, 034903 (2014).

[16] A. Adare *et al.* (PHENIX Collaboration), Nuclear matter effects on J/ψ production in asymmetric Cu + Au collisions at $\sqrt{s_{NN}} =$ 200 GeV, Phys. Rev. C **90**, 064908 (2014).

[17] S. S. Adler *et al.* (PHENIX Collaboration), Production of ϕ mesons at midrapidity in $\sqrt{s_{NN}} = 200$ GeV Au+Au collisions at RHIC, Phys. Rev. C **72**, 014903 (2005).

[18] A. Adare *et al.* (PHENIX Collaboration), Nuclear modification factors of ϕ mesons in d+Au, Cu + Cu and Au+Au collisions at $\sqrt{s_{NN}} = 200$ GeV, Phys. Rev. C **83**, 024909 (2011).

[19] A. Adare *et al.* (PHENIX Collaboration), Measurement of neutral mesons in $p+p$ collisions at $\sqrt{s} = 200$ GeV and scaling properties of hadron production, Phys. Rev. D **83**, 052004 (2011).

[20] A. Adare *et al.* (PHENIX Collaboration), Low-mass vector-meson production at forward rapidity in $p+p$ collisions at $\sqrt{s} =$ 200 GeV, Phys. Rev. D **90**, 052002 (2014).

[21] B. I. Abelev *et al.* (STAR Collaboration), Partonic Flow and ϕ-Meson Production in Au+Au Collisions at $\sqrt{s_{NN}} = 200$, Phys. Rev. Lett. **99**, 112301 (2007).

[22] B. I. Abelev *et al.* (STAR Collaboration), Energy and system size dependence of ϕ meson production in Cu + Cu and Au+Au collisions, Phys. Lett. B **673**, 183 (2009).

[23] J. Adam *et al.* (ALICE Collaboration), ϕ-meson production at forward rapidity in p-Pb collisions at $\sqrt{s_{NN}} = 5.02$ TeV and in pp collisions at $\sqrt{s} = 2.76$ TeV, arXiv:1506.09206.

[24] B. B. Abelev *et al.* (ALICE Collaboration), $K^*(892)^0$ and $\phi(1020)$ production in Pb−Pb collisions at $\sqrt{s_{NN}} = 2.76$ TeV, Phys. Rev. C **91**, 024609 (2015).

[25] K. Adcox *et al.* (PHENIX Collaboration), PHENIX detector overview, Nucl. Instrum. Methods Phys. Res., Sec. A **499**, 469 (2003).

[26] H. Akikawa *et al.* (PHENIX Collaboration), PHENIX muon arms, Nucl. Instrum. Methods Phys. Res., Sec. A **499**, 537 (2003).

[27] M. Allen *et al.* (PHENIX Collaboration), PHENIX inner detectors, Nucl. Instrum. Methods Phys. Res., Sec. A **499**, 549 (2003).

[28] A. Taketani *et al.* (PHENIX Collaboration), Silicon vertex tracker for RHIC PHENIX experiment, Technology and instrumentation in particle physics. Proceedings, 1st International Conference, TIPP09, Tsukuba, Japan, March 12-17, 2009, Nucl. Instrum. Methods Phys. Res., Sec. A **623**, 374 (2010).

[29] C. Aidala *et al.*, The PHENIX Forward Silicon Vertex Detector, Nucl. Instrum. Methods Phys. Res., Sec. A **755**, 44 (2014).

[30] C. Baglin *et al.* (NA38 Collaboration), The production of J/ψ in 200-GeV/nucleon oxygen uranium interactions, Phys. Lett. B **220**, 471 (1989).

[31] A. Adare *et al.* (PHENIX Collaboration), J/ψ suppression at forward rapidity in Au+Au collisions at $\sqrt{s_{NN}} = 200$ GeV, Phys. Rev. C **84**, 054912 (2011).

[32] T. Sjostrand, P. Eden, C. Friberg, L. Lonnblad, G. Miu, S. Mrenna, and E. Norrbin, High-energy physics event generation with PYTHIA 6.1, Comput. Phys. Commun. **135**, 238 (2001).

[33] R. Brun, F. Carminati, and S. Giani, GEANT detector description and simulation tool, CERN-W5013, 1994.

[34] J. Beringer *et al.* (Particle Data Group Collaboration), Rev. of Particle Phys. (RPP), Phys. Rev. D **86**, 010001 (2012).

[35] L.-W. Chen and C. M. Ko, Anisotropic flow in Cu + Au collisions at $\sqrt{s_{NN}} = 200$ GeV, Phys. Rev. C **73**, 014906 (2006).